




## Article

# Aluminum Oxide Coatings as Nanoadsorbents for the Treatment of Effluents Colored with Eriochrome Black T

Gustavo R. Kramer <sup>1,2,3</sup> , Florencia A. Bruera <sup>1,2,4</sup>, Pedro Darío Zapata <sup>1,2,4</sup>  and Alicia E. Ares <sup>1,2,3,\*</sup> 

<sup>1</sup> Facultad de Ciencias Exactas, Químicas y Naturales, Universidad Nacional de Misiones, Buenos Aires 3300, Argentina; grkramer@fceqyn.unam.edu.ar (G.R.K.); brueraflorescia@gmail.com (F.A.B.); pedro.zapata@unam.edu.ar (P.D.Z.)

<sup>2</sup> Consejo Nacional de Investigaciones Científicas y Técnicas (CONICET), Buenos Aires 2290, Argentina

<sup>3</sup> Programa de Materiales y Fisicoquímica (PROMyF), Instituto de Materiales de Misiones (IMaM-CONICET), Buenos Aires 3300, Argentina

<sup>4</sup> Laboratorio de Biotecnología Molecular, Instituto de Biotecnología Misiones “Dra. María Ebe Reca” (INBIOMIS), Garupá 3304, Argentina

\* Correspondence: aares@fceqyn.unam.edu.ar; Tel.: +54-376-442-2186 or +54-376-449-7141

**Abstract:** The contamination of water bodies with toxic compounds from the agricultural, industrial, and domestic sectors is a serious environmental problem. Adsorption is one of the simplest, most functional, and economical methods for treating large volumes of water and removing its contaminant load. Thanks to its nanoporous structure, versatility, chemical inertness, and low-cost synthesis, anodic aluminum oxide (AAO) can be used as an adsorbent in a wide range of applications. In this work, nanostructured AAO coatings were successfully synthesized, and their performance as adsorbents was evaluated in decolorization tests of Eriochrome Black T (EBT) solutions. The adsorption process was found to be dependent on the initial dye concentration, agitation, temperature, and contact time. At 25 °C and 16 mg·L<sup>−1</sup> initial EBT concentration, a maximum removal efficiency (%R) of 78% was obtained after 4.5 h at 500 rpm and after 5.5 h at 100 rpm, while without agitation, after 8.3 h of treatment, the highest %R was 40%. Furthermore, the adsorption rate increased significantly with temperature, reaching a %R of 99% after 2.25 h at 60 °C and 500 rpm. Additionally, it was demonstrated that the adsorbent can be used up to four times with a removal efficiency greater than 50%.

**Keywords:** nanoporous aluminum oxide; adsorption; Eriochrome Black T



Academic Editor: Ioannis Pashalidis

Received: 24 March 2025

Revised: 14 April 2025

Accepted: 18 April 2025

Published: 20 April 2025

**Citation:** Kramer, G.R.; Bruera, F.A.; Zapata, P.D.; Ares, A.E. Aluminum Oxide Coatings as Nanoadsorbents for the Treatment of Effluents Colored with Eriochrome Black T. *Coatings* **2025**, *15*, 488. <https://doi.org/10.3390/coatings15040488>

**Copyright:** © 2025 by the authors. Licensee MDPI, Basel, Switzerland. This article is an open access article distributed under the terms and conditions of the Creative Commons Attribution (CC BY) license (<https://creativecommons.org/licenses/by/4.0/>).

## 1. Introduction

The rapid growth of industrial activities has increased the amount of wastewater containing highly toxic and environmentally harmful pollutants, such as dyes, heavy metals, agricultural products, and pharmaceuticals [1–3]. Dyes mainly used industrially in textile and paint manufacturing, printing, and leather production constitute a significant portion of these degradation-resistant chemical species [4,5]. To understand the magnitude of this problem, the textile industry alone releases approximately 100,000 tons of dyes into wastewater annually [6–11], with azo dyes being the most widely used [12,13]. Due to their recalcitrant, carcinogenic nature and long-term effect on ecosystems, it is essential to remove these contaminants before their discharge into water bodies [12,14,15]. Eriochrome Black T (EBT), used in the dyeing of multifibers, nylon, wool, and silk, can be considered a representative model of anionic azo dyes [10].

Several technologies, such as adsorption, coagulation, advanced oxidation, membrane separation, biological treatments, and ozonation, can be used to remove dyes from

industrial effluents [15–17]. Of these, adsorption is one of the most effective advanced wastewater treatments for the removal of hazardous inorganic and organic pollutants from effluents due to its ease of operation, high efficiency, and low cost [14,18–20]. In addition, this technology can be used to treat various types of pollutants [21,22] and can be easily integrated into existing water treatment systems [23].

Adsorption occurs due to the migration of the dye from the bulk solution to the solid surface by sharing or exchange of electrons, called chemisorption, or by weak interaction forces, such as van der Waals forces, reported as physisorption [23,24]. According to [25], adsorption can be described through four fundamental steps: (1) diffusion of molecules from the fluid to the fluid boundary layer near the adsorbent, (2) diffusion through said fluid boundary layer, (3) adsorption onto the active sites, and finally, (4) intraparticle diffusion or diffusion through the pores into the pores.

Khalid et al. [14] highlight that the selection of the adsorbent and its operating conditions in the adsorption process are key to achieving maximum pollutant removal. There is a wide variety of adsorbents applied for the removal of dyes from wastewater are clays minerals, zeolites, composites, various agro-industrial wastes, inorganic nanomaterials, metal-organic frameworks and metal oxides [14,15,26].

Among metal oxides, anodic aluminum oxide (AAO) can be considered a potential adsorbent for dye removal from water in the form of a nanoporous film/coating. This nanomaterial, notable for its high surface area and chemical resistance [27–29], can be easily and inexpensively synthesized by anodic oxidation, producing a film with closely packed pores on the substrate acting as an anode. This provides great versatility for forming parts with complex configurations that function as fillers or as part of adsorption equipment applied at different scales. Furthermore, to date, only the adsorbent capacity of aluminum oxide nanoparticles has been studied [15,17,24], while AAO coatings have the advantage of easy separation and recovery.

In this work, the decolorization of EBT-colored solutions was studied using an innovative material, nanostructured anodic aluminum oxide. To this end, AAO coatings were synthesized by anodic oxidation from a commercial aluminum alloy, and the influence of stirring and temperature on the adsorption of the dye was studied. The kinetics and physicochemical properties of the adsorption process were also analyzed to understand its fundamentals and mechanisms.

## 2. Materials and Methods

### 2.1. Synthesis of the Nanoporous Anodic Aluminum Oxide

A sheet of the commercial aluminum alloy AA1050 (99.5% Al, supplied by AMEX<sup>®</sup> S.A., Ciudad de Buenos Aires, Argentina) with 0.3 cm thickness, 1 cm wide and 15 cm long was used as the substrate.

Prior to anodization, the edges of the substrate were grinded in a rotary plate polisher (Struers, Singapore) at 250 rpm, with SiC sandpapers of decreasing grit size from #280 to #2500 (Double A and Norton, Buenos Aires, Argentina). The substrate was then cleaned with a mixture of distilled water and ethanol for about 5–10 min in an ultrasound and bent into a spiral shape prior to anodization.

AAO coatings were synthesized in triplicate by a single 1 h anodization step in 0.3 M oxalic acid at 40 °C and 30 V, as reported by Bruera et al. [27,28].

After anodic oxidation, the edge of the sample that was not anodized in the electrochemical process was cut off to obtain fully OAA-coated samples.

## 2.2. Preparation of EBT Dye Solutions

Aqueous solutions of eriochrome black T were prepared at a concentration of  $400 \text{ mg}\cdot\text{L}^{-1}$ . From this stock solution, serial dilutions were performed to obtain the desired concentrations using distilled water. The exact concentration of the dyes was obtained using a UV-visible spectrophotometer (Shimadzu UV-1800, Kyoto, Japan). The EBT calibration curve was constructed from several dilutions of the stock solution, using a range of concentrations between 10 and  $50 \text{ mg}\cdot\text{L}^{-1}$ . The variation of the dye concentration vs. absorbance showed a linear behavior at  $\lambda_{\text{max}} = 528 \text{ nm}$ , and the linear regression equation was  $y = 0.0183x - 0.0017$ , with a high correlation coefficient ( $R^2 = 0.998$ ). The concentrations of EBT in the solutions before and after equilibrium adsorption were determined from the calibration curve.

## 2.3. Characterization of AAO Coatings

The nanopores in the anodic films were characterized by scanning electron microscopy (SEM) (SUPRA 40, Carl Zeiss NTS GmbH, Jena, Germany). Pore Diameter (PD), pore Density (D), and Porosity (P) were determined from SEM micrographs, and thickness (T) was determined with an optical microscope (EPIPHOT, Nikon, Tokyo, Japan), as reported by Bruera et al. [27–29].

In addition, SEM images of the AAO coatings were taken after 24 h of EBT adsorption, and their elemental composition and content were studied using an energy-dispersive spectrometer (EDS).

To determine surface functional groups, Fourier transform infrared (FTIR) analyses were performed using the IRPrestige-21 instrument (Shimadzu, Kyoto, Japan) in the  $4000\text{--}600 \text{ cm}^{-1}$  region.

## 2.4. Adsorption Assays

### 2.4.1. Preliminary Studies

The adsorption experiments were performed in triplicate at different temperatures ( $25\text{--}60 \text{ }^\circ\text{C}$ ) in a 100 mL beaker containing 30 mL of EBT dye solution ( $C = 16 \text{ mg}\cdot\text{L}^{-1}$ ) and a spiral-mounted AAO adsorbent with a total area of  $30 \text{ cm}^2$ . Dye concentration was determined by UV-Vis spectrophotometry at different contact times (0–24 h).

From the data obtained, the removal efficiency (%R), the adsorption capacity at equilibrium ( $q_e$ ), and the adsorption capacity at a given time ( $q_t$ ) were calculated using Equations (1)–(3) [2,17,30].

$$R(\%) = \frac{C_0 - C_t}{C_0} \times 100 \quad (1)$$

$$q_e = \frac{(C_0 - C_e) \times V}{a} \quad (2)$$

$$q_t = \frac{(C_0 - C_t) \times V}{a} \quad (3)$$

where  $C_0$  is the adsorbate initial concentration ( $\text{mg}\cdot\text{L}^{-1}$ ),  $C_t$  and  $C_e$  are the adsorbate final concentration after time  $t$  and at equilibrium ( $\text{mg}\cdot\text{L}^{-1}$ ),  $V$  is the volume of solution (L) and  $a$  is the effective adsorption surface area ( $\text{cm}^2$ ).

The effect of stirring on the removal efficiency and  $q_e$  at different contact times was evaluated, performing experiments under static conditions and magnetic stirring at 100 and 500 rpm.

### 2.4.2. Kinetic Adsorption Models

The kinetic study was performed at  $25 \text{ }^\circ\text{C}$  and 500 rpm. Several kinetic models, including pseudo first-order (PFO), pseudo second-order (PSO), intraparticle diffusion

(IPD) and Boyd's external diffusion (ED) models, were used to determine the EBT removal performance of the nanoadsorbent.

The kinetic data were tested according to the linearized models and compared based on the value of the correlation factor ( $R^2$ ). The kinetic model equations are provided in Table 1 [2,30–33].

**Table 1.** Kinetic models.

Models	Linear Form
Lagergren Pseudo-first-order	$\ln(q_e - q_t) = \ln q_e - k_1 t$
Ho-McKay Pseudo-second-order	$\frac{t}{q_t} = \frac{1}{k_2 q_e^2} + \frac{t}{q_e}$
Weber-Morris Intra-particle diffusion	$q_t = k_{id} t^{0.5} + I$
Boyd's external diffusion	$\ln\left(1 - \frac{q_t}{q_e}\right) = -k_3 t + A$

Here,  $k_1$  represents the PFO rate constant ( $\text{min}^{-1}$ ),  $t$  (min) is the time,  $k_2$  is the PSO rate constant ( $\text{cm}^2 \cdot \text{mg}^{-1} \cdot \text{h}^{-1}$ ),  $k_{id}$  ( $\text{mg} \cdot \text{cm}^{-2} \cdot \text{h}^{-0.5}$ ) is the IPD rate constant and  $I$  is the proportional to the boundary layer and  $k_3$  ( $\text{min}^{-1}$ ) and  $A$  are liquid film diffusion constants.

#### 2.4.3. Isotherm Adsorption Models

The dye adsorption isotherms were determined under the same conditions as the kinetics experiments, but using different initial EBT concentrations (between 5–50  $\text{mg} \cdot \text{L}^{-1}$ ). A contact time of 24 h was applied to be sure that the equilibrium is reached for higher concentrations. Three different isotherm models were tested to interpret the data obtained from experimental studies. The mathematical equations of these models are presented in Table 2 [17,30].

**Table 2.** Isotherm models.

Models	Linear Form
Freundlich	$\ln q_e = \ln k_f + \frac{1}{n} \ln C_e$
Temkin	$q_e = B \ln k_t + B \ln C_e$
Langmuir	$\frac{C_e}{q_e} = \frac{C_e}{q_{max}} + \frac{1}{k_L q_{max}}$

Where  $k_f$  ( $\text{mg}^{1-(1/n)} \cdot \text{L}^{1/n} \cdot \text{cm}^2$ ) is the Freundlich constant and  $n$  is the heterogeneity factor,  $k_t$  ( $\text{L} \cdot \text{cm}^{-2}$ ) is the equilibrium binding constant corresponding to the maximum binding energy and  $B$  ( $\text{J} \cdot \text{mol}^{-1}$ ) is the constant related to the heat of adsorption and  $k_L$  ( $\text{L} \cdot \text{mg}^{-1}$ ) is the Langmuir constant and  $q_{max}$  ( $\text{mg} \cdot \text{cm}^{-2}$ ) is the maximum adsorption capacity.

#### 2.4.4. Thermodynamic Studies

Equations (4)–(6) [25,34] were used to estimate the thermodynamic variables, including changes in the Gibbs free energy ( $\Delta G^\circ$ ) ( $\text{KJ} \cdot \text{mol}^{-1}$ ), free enthalpy ( $\Delta H^\circ$ ) ( $\text{KJ} \cdot \text{mol}^{-1}$ ), and entropy ( $\Delta S^\circ$ ) ( $\text{KJ} \cdot \text{mol}^{-1} \cdot \text{K}^{-1}$ ):

$$\Delta G^\circ = -RT \ln K_c \quad (4)$$

$$\Delta G^\circ = \Delta H^\circ - T \Delta S^\circ \quad (5)$$

$$\ln K_c = \frac{\Delta S^\circ}{R} - \frac{\Delta H^\circ}{RT} \quad (6)$$

Here ( $R = 8.314 \text{ J} \cdot \text{mol}^{-1} \cdot \text{K}^{-1}$ ) is the universal gas constant,  $T$  (K) is the temperature used and  $K_c$  is the thermodynamic equilibrium constant. The change in  $\Delta H^\circ$  and  $\Delta S^\circ$  can be obtained from the slope and intercept of the plot of  $\ln K_c$  versus  $T^{-1}$  using the Van't Hoff formula presented in (Equation (6)).

#### 2.4.5. Reuse Performance

Adsorbent reuse studies were carried out with an initial EBT concentration of 16  $\text{mg} \cdot \text{L}^{-1}$ , at 500 rpm and 50 °C, and with a contact time of 2 h. After adsorption, the OAA samples were washed with 40 mL of a 0.1 M NaOH solution for 10 min, under stirring and



at room temperature. The samples were then immersed in a 0.1 M HCl solution to achieve neutralization. This adsorption-desorption process was performed up to four times, and the %R was measured for each use.

### 3. Results and Discussion

#### 3.1. Characteristic of AAO Films

SEM images of anodic aluminum oxide coatings synthesized by a single anodization step in 0.3 M oxalic acid at 40 °C and 30 V (Figure 1a,b) show a regular structure of disordered and variable-sized nanopores with PDs ranging from approximately 3–35 nm. This means that the elimination of some surface smoothing treatments, post-anodization etching, and a second anodization are detrimental to the long-range order in the nanostructure, as reported by Bruera et al. [27,28]. However, it was possible to obtain low-cost AAO nanostructured films with morphological characteristics similar to those obtained by Bruera et al. [27,28] with  $PD = 27.34 \pm 10.11$  nm,  $D = 2.04 \times 10^{10} \pm 4.1 \times 10^9$  pores.  $\text{cm}^{-2}$ ,  $P = 21.24 \pm 3.72\%$  and  $T = 19.83 \pm 0.75$   $\mu\text{m}$  for use as nanoadsorbents.

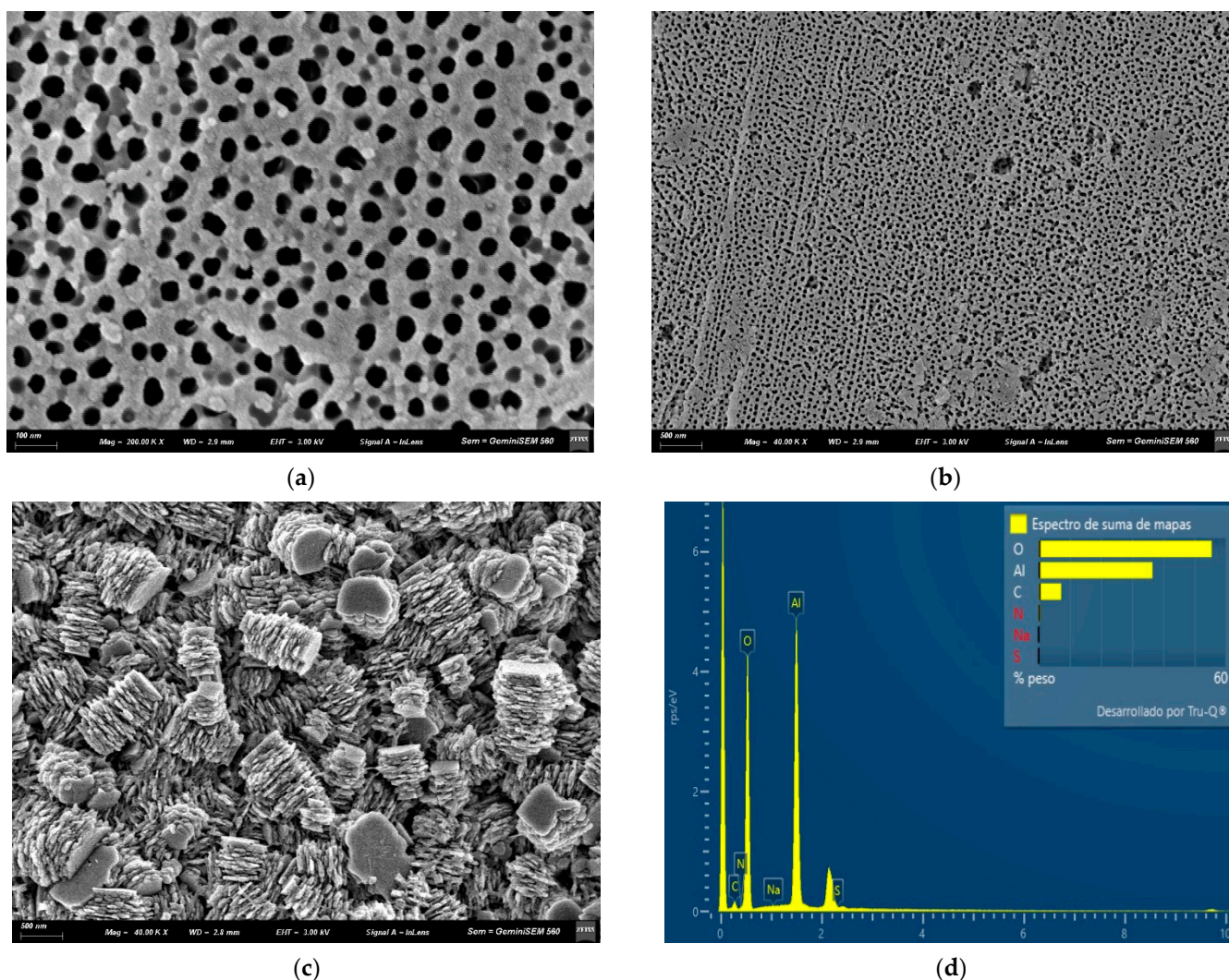


**Figure 1.** SEM micrographs of AAO coatings synthesized in 0.3 M at 40 °C and 30 V before adsorption (a,b) and after adsorption with EDX analysis (c,d).

On the other hand, the SEM image of the AAO after 24 h of contact time with EBT (Figure 1c) shows the adsorption of the dye over the entire surface of the material, completely covering the nanopores due to the stacking of the dye molecules.

In addition, the EDX spectrum in Figure 1d indicated high-intensity peaks for O and Al, corresponding to OAA, and lower-intensity peaks for C, N, Na, and S, corresponding to the azo dye EBT. The layer of dye adsorbed on the surface could be relatively thin, given the depth of the EDX analysis (1–2  $\mu\text{m}$ ).

FTIR spectroscopy results for the AAO before and after EBT adsorption (Figure 2) demonstrate the presence of several peaks in the range of 600–4000  $\text{cm}^{-1}$ , which define the chemical properties and functional groups of the adsorbent and adsorbate molecules.

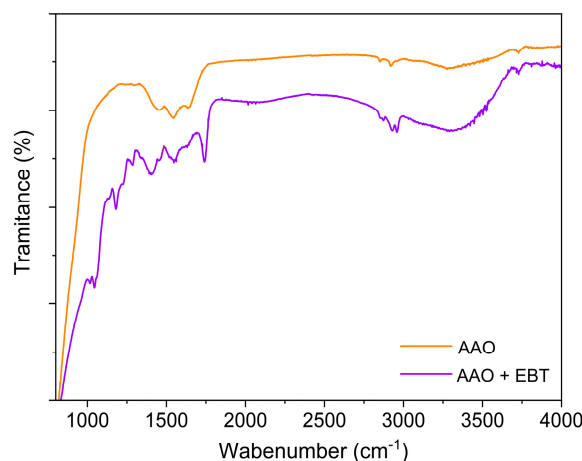


**Figure 2.** FTIR spectra for the AAO before and after EBT adsorption.

For both cases, a broad band was observed in the region from 3000 to 3700  $\text{cm}^{-1}$  (around 3309  $\text{cm}^{-1}$ ), characteristic of the stretching vibration of the O-H group from Al-OH, and a peak at 1641  $\text{cm}^{-1}$  typical of the bending vibrations of the O-H groups [14,15,35,36]. Likewise, the peaks in the 1250 to 1600  $\text{cm}^{-1}$  region may be due to C-N stretching, N-H bending (in the case of the AAO + EBT curve), and Al-OH bending (for both cases) [37]. In the AAO + EBT curves the peaks at 2959, 2932 and 2870  $\text{cm}^{-1}$  represent the C-H stretching vibration in the  $\text{CH}_2$ ,  $\text{CH}_3$ , or  $\text{N-CH}_3$  groups [35], while those located at 1740  $\text{cm}^{-1}$  and around 1100  $\text{cm}^{-1}$  can be attributed to the C=O group [36] and the C=C and C-O groups [14], respectively. These results show the interaction between the EBT dye molecules and the functional groups present on the surface of the OAA.

### 3.2. Adsorption Studies

#### 3.2.1. Influence of Agitation, Initial Concentration, and Temperature on EBT Adsorption

Many studies have reported a significant effect of agitation and temperature on the adsorption of organic compounds [38,39]. Figure 3 represents the impact of contact time on the EBT removal efficiency and adsorption capacity of AAO films at different agitation speeds and temperatures. This figure shows a significant increase in dye adsorption over time and as the agitation speed and temperature increase.

In particular, the absence of agitation during the EBT adsorption process on aluminum oxide (Figure 3a,b) reduces the removal rate compared to the curves obtained at 100 and 500 rpm, reaching a maximum removal efficiency of 40% in 500 min (approximately 8.3 h). This could be due to a removal rate controlled by the diffusion of dye particles to the adsorbent/adsorbate interface.

On the other hand, stirring the solution at 100 and 500 rpm allows reaching maximum removal efficiencies of 78% in a time of 500 min, almost double compared to the test without agitation at the same time, and reaching the equilibrium condition in less time. Therefore, agitation can increase the diffusion rate of dye particles from the fluid to the boundary

layer in contact with the AAO, due to the formation of turbulence and the decrease in the thickness of the fluid boundary layer [39].

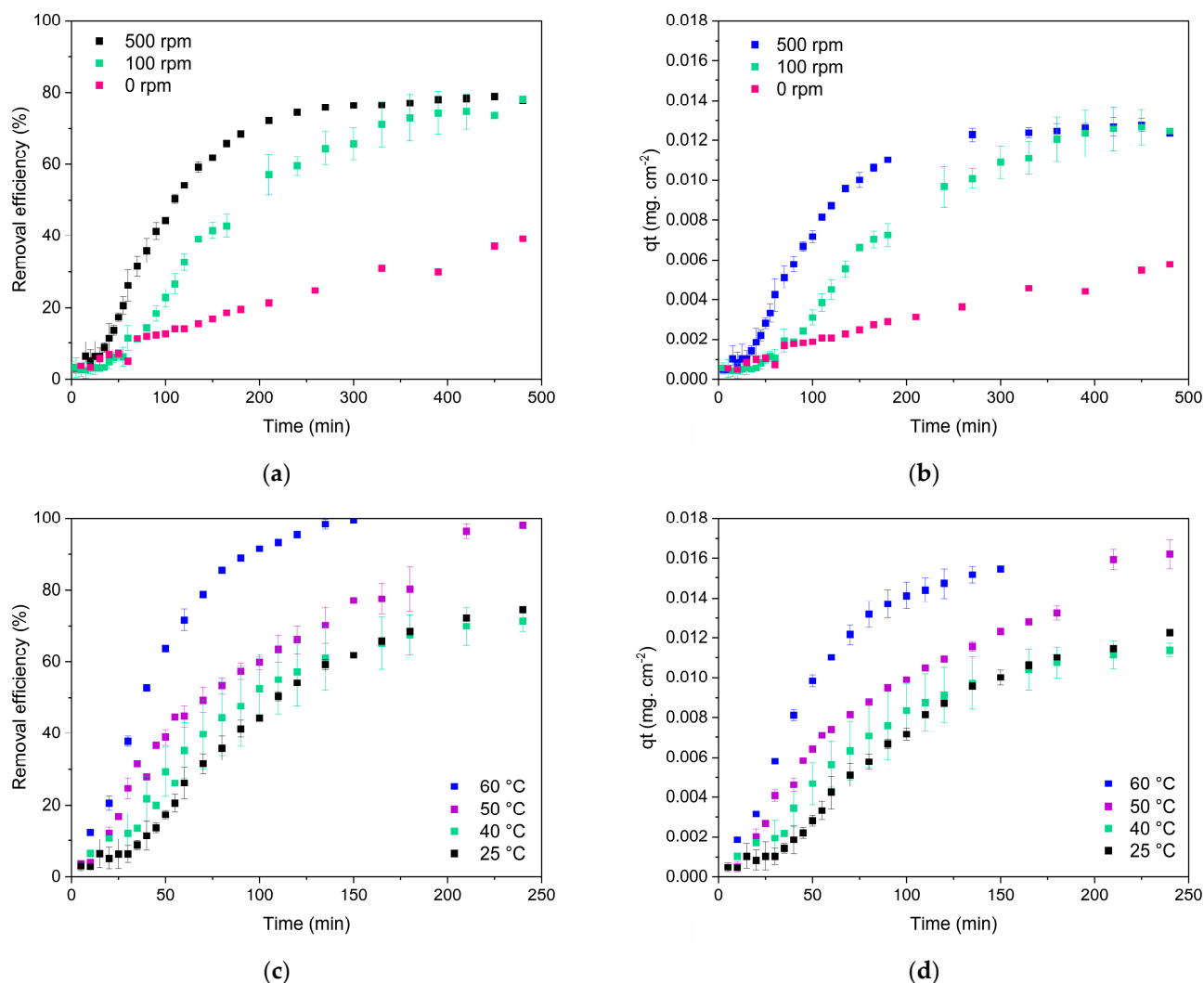


**Figure 3.** Effect of contact time on EBT removal efficiency and  $q_t$  ( $C_0 = 16 \text{ mg} \cdot \text{L}^{-1}$ ) at different agitation levels (a,b) and temperatures (c,d).

Furthermore, the removal efficiency and  $q_t$  curves for the tests with agitation speeds of 100 and 500 rpm (Figure 3a,b) showed three distinct zones: (1) low speed, (2) high speed, and (3) constant speed.

The low-speed zone is characterized by  $R\%$  and  $q_t$  values close to 0 and occurs during the first 35 min of contact time at 100 rpm and during the first 10 min at 500 rpm. The low initial speed may be due to the fact that moving systems can generate a fluid boundary layer near the adsorbent surface, where dye diffusion occurs at a specific rate and can be limiting in the adsorption process [40].

The high-speed zone is characterized by a high slope until reaching the equilibrium state, where maximum values of  $\%R$  and  $q_t$  are reached and remain constant over time. It is worth noting that increasing the stirring speed from 100 to 500 rpm significantly increases the slope in this area of the curve, and thus the dye removal rate. This means that maximum values of  $\%R$  and  $q_t$  are reached at 4.5 h at 500 rpm and at 5.5 h at 100 rpm. This high-velocity zone could be due to an increase in the dye concentration gradient in the boundary layer, with the consequent increase in diffusion and availability of a large number of active sites on the adsorbent surface. [33]. Finally, the constant-speed zone can

be explained by the saturation of the adsorbent and the competition of the adsorbate for the remaining active sites.

It is interesting to note that during adsorption, the adsorbent does not disperse in solution as occurs with agitated particulate adsorbents. This may be a determining factor in the adsorption rate when comparing different types of adsorbents. For example, Gaayda et al. [15] evaluated the adsorption of EBT onto aluminum oxide nanoparticles and obtained maximum removal efficiency (71%) and  $q_e = 45 \text{ mg}\cdot\text{g}^{-1}$  for a dosage of 0.05 g of particles per 50 mL of EBT solution ( $C_0 = 100 \text{ mg}\cdot\text{L}^{-1}$ ) after 100 min at 150 rpm and 50 °C. Similarly, but using methylene blue as a dye, Sangor and Al-Ghouti [36] obtained  $q_e$  values close to  $80 \text{ mg}\cdot\text{g}^{-1}$  after 24 h and at 25 °C for the same dosage of aluminum oxide nanoparticles and stirring speed. On the other hand, Balloy et al. [17] obtained an improved adsorption capacity ( $q_e$  between 344 and  $402 \text{ mg}\cdot\text{g}^{-1}$ ) for the adsorption of EBT with pseudo-boehmite ( $\gamma\text{-AlOOH}$ ) and gamma alumina ( $\gamma\text{-Al}_2\text{O}_3$ ) nanoparticles, reaching the maximum removal efficiency (100 %) at 20 min and 25 °C. As can be noticed, there are no studies to date that evaluate the potential of nanoporous AAO as an adsorbent in its presentation as a coating/film and non-particulate form, with the advantage that it can be easily recovered from the solution to be treated.

Figure 3c,d show the influence of increasing the temperature of the dye solution from 25 to 60 °C at a constant stirring speed of 500 rpm. These results demonstrate a progressive increase in the %R and  $q_t$  values with temperature, reaching almost total EBT removal (%R = 99%) after 2.25 h at 60 °C. This could be due to the fact that increasing temperature can enhance the mobility of the dye molecules, modify the energy and quantity of active sites, and alter the adsorbent/adsorbate interaction [41,42].

On the other hand, the shapes of these curves change particularly in the initial interval between 0 and 10 min for temperatures above 25 °C, where the disappearance of the low-velocity zone is observed as temperature increases (increase in the initial slope). This behavior could be associated with the decrease in the boundary layer and increased diffusion of EBT molecules through it. Furthermore, the error bars presented in Figure 3c,d show similar slopes in the high-velocity zone for temperatures of 25–40 and 40–50 °C, and the equilibrium %R and  $q_t$  values occur at 4 h of exposure with the dye.

Finally, the increase in adsorption capacity with temperature suggests that the adsorption process is endothermic [33], and this result can be compared with the thermodynamic parameters analyzed in Section 3.2.4.

The effect of the initial adsorbate concentration in solution is decisive for evaluating the effectiveness of the adsorption process [2]. Figure 4 illustrates the variation of %R and  $q_e$  with the initial dye concentration after 24 h of adsorption at 500 rpm and 25 °C.

The increase in the initial concentration of EBT and the consequent rise in the concentration gradient generate a reduction in the resistance to mass transfer, which improves the adsorption process. This explains why the  $q_e$  values increase with the initial concentration of EBT [2,43]. Likewise, the decrease in %R with increasing initial EBT concentration is an effect attributed to the repulsive electrostatic interaction between the EBT molecules in solution and those adsorbed on the OAA surface [44,45].



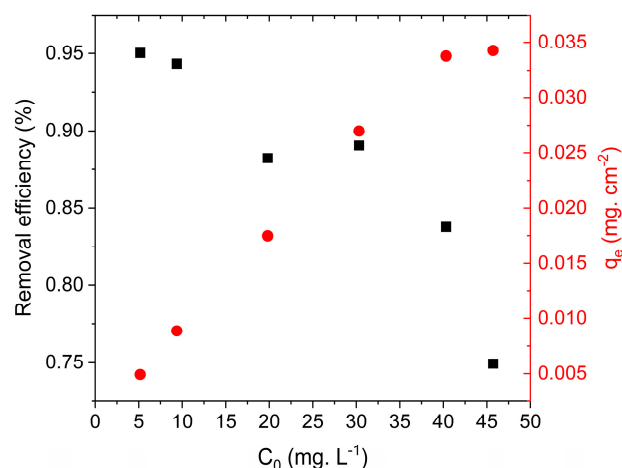


**Figure 4.** Removal efficiency and  $q_e$  at different EBT initial concentrations after 24 h of adsorption at 500 rpm and 25 °C.

### 3.2.2. Adsorption Kinetics

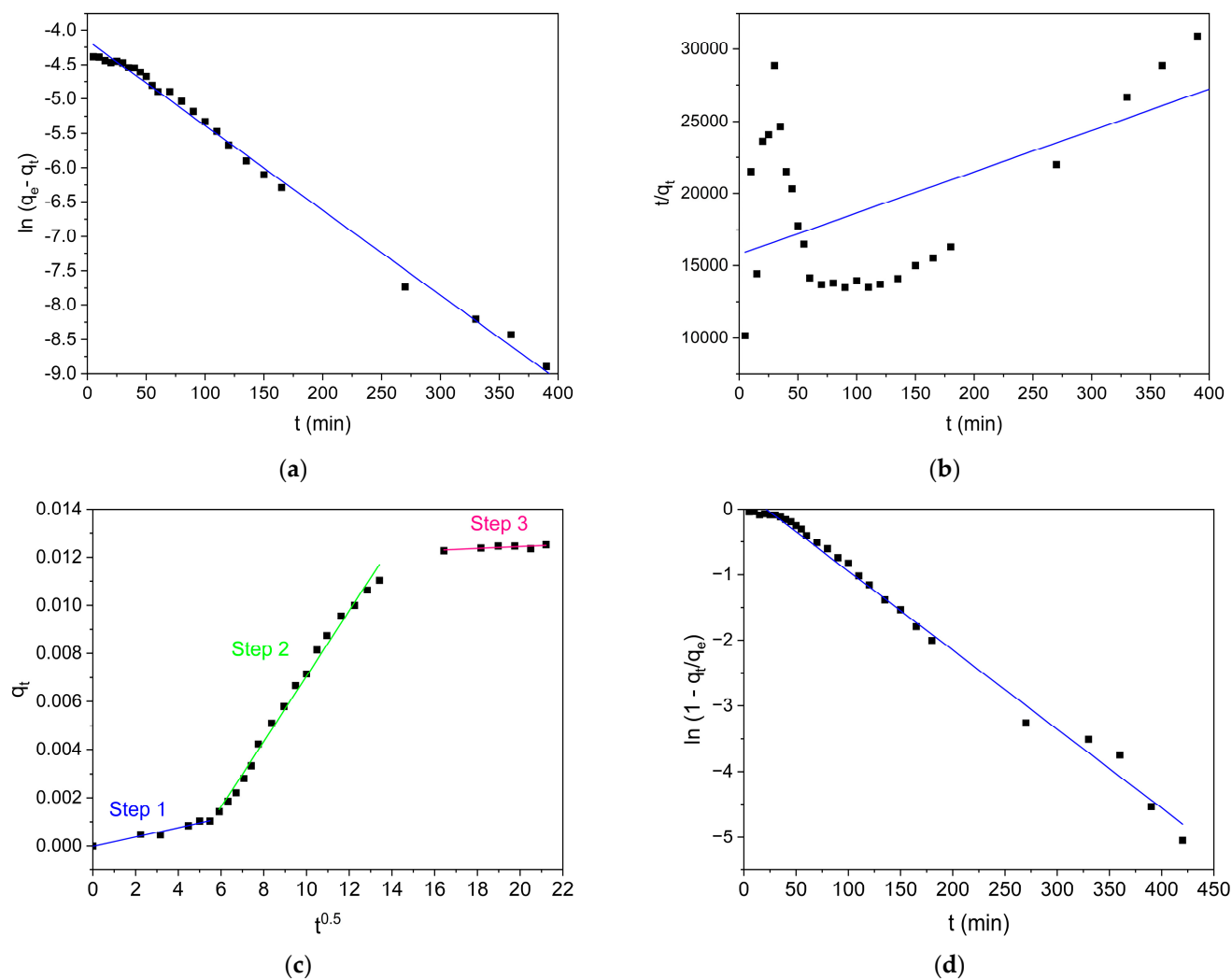
The study of adsorption kinetics can be significant for understanding the mechanisms involved and the physicochemical characteristics of the process [30]. In this case, the analysis of the adsorption kinetics of EBT on AAO films was performed by fitting the results obtained to four kinetic models: pseudo-first-order kinetic (PFO), pseudo-second-order kinetic (PSO), intra-particle diffusion model (IPD), and the external diffusion model (ED) [32,46].

Figure 5 shows the experimental curves and the fits of the proposed models, and Table 3 represents the values of the corresponding fitting parameters.

**Table 3.** Kinetic parameters of different adsorption models at 16 mg·L<sup>-1</sup> initial EBT concentrations.

Models	Parameters	
Pseudo-first-order	$R^2$	0.9912
	$k_1$	0.0120
	$q_e$	0.0165
Pseudo-second-order	$R^2$	0.3058
	$k_2$	0.0517
	$q_e$	0.0350
Intra-particle diffusion *	$R^2_1$	0.9629
	$k_{id\ 1}$	0.0002
	$I_1$	0.00005
	$R^2_2$	0.9947
	$k_{id\ 2}$	0.0014
	$I_2$	0.0072
	$R^2_3$	0.8352
	$k_{id\ 3}$	0.0002
	$I_3$	0.0082
Boyd's external diffusion	$R^2$	0.9926
	$k_3$	0.0122
	$A$	0.2936

\* The subscript corresponds to the adjustment applied to each linear segment of the curve.



**Figure 5.** Linear representation of the data fitted into the different models of adsorption kinetics: (a) PFO, (b) PSO, (c) IPD, and (d) ED models.

According to the correlation coefficient  $R^2$  values for the PFO and PSO model fits (Table 3), the adsorption process of EBT onto AAO under the studied conditions was best explained by assuming that the adsorption rate follows a first-order reaction. This would explain why the adsorption process is not controlled by adsorption at the active sites, since EBT molecules identify all the adsorption sites on the AAO surface as a single group [40].

Furthermore, the PFO model can represent the external/internal diffusion, and it is more suitable for describing the kinetics of the initial adsorption stage, but cannot accurately describe the entire adsorption process [30,46].

In this sense, the data in Table 3 demonstrate that the  $q_e$  value predicted using the PFO model (determined as the slope of the graph) was closer to that of the adsorption equilibrium obtained experimentally, thus reinforcing the kinetic model proposed previously.

The data fit with the IPD model shows that  $q_t$  vs.  $t^{0.5}$  is not a straight line passing through the origin (0.0), so it can be concluded that adsorption is controlled by multiple processes [17,31,46,47]. This same model was used to fit up to three linear segments, indicating that the adsorption process occurs and dominates under three stages (Figure 5c). The fitting values corresponding to each segment presented in Table 3 have a high correlation coefficient  $R^2$  (close to unity). This represents a good approximation and is consistent with the adsorption stages explained in Section 3.2.1.

In this sense, the first stage indicates a slow initial exterior surface dye adsorption onto the surface of the adsorbent correlated with external mass transfer. As discussed above, the agitation effect is significant and enhances the diffusion of molecules from the solution to the fluid boundary layer, making the first adsorption step rapid and its analysis unnecessary [25]. Therefore, this segment or stage corresponds solely to the boundary layer diffusion control.

The second step corresponds to intraparticle diffusion and binding of EBT molecules to the active sites of AAO. However, compared to the first step, this stage is faster ( $k_{id1} > k_{id2}$ ) but still rate-limiting [15,42,46,48,49].

Finally, the third step is a plateau, which may indicate the equilibrium process and subsequent saturation of the adsorbent, which is reflected by a decrease in the diffusion rate due to the decrease in dye concentration [48,50].

The fit of the film diffusion model, represented by  $\ln(1 - q_t/q_e)$  versus  $t$  in Figure 5d and by the  $R^2$  values in Table 3, indicated that EBT diffusion through the liquid boundary layer near the AAO surface can be considered one of the most limiting steps and has the greatest effect on the overall rate of the adsorption process under the selected conditions. These preliminary conclusions are in agreement with previous discussions on the fitting of the PFO and IPD models [25,32,47].

### 3.2.3. Adsorption Isotherm

Adsorption isotherms express at a constant temperature the relationship between the adsorbate concentration and its degree of accumulation on the adsorbent [30]. Therefore, the analysis of adsorption isotherms provides a better understanding of the mechanisms involved in adsorption and the performance of the overall process. [42].

In this study, the following three commonly used isotherm models were compared: the Freundlich, Temkin, and Langmuir models [15]. The fitting results and parameters of each model are shown in Table 4. A graphical representation of the data is shown in Figure 6.

**Table 4.** Parameters and the equations of the model at 25 °C.

Models	Linear Fitting Formula	Parameters	
Freundlich	$0.5316x - 4.4641$	$R^2$	0.9626
		$k_f$	0.0115
		$n$	1.8811
Temkin	$0.0084x + 0.0149$	$R^2$	0.9521
		$k_t$	5.8932
		$B$	0.0084
Langmuir	$24.212x + 50.814$	$R^2$	0.9805
		$q_{max}$	0.0413
		$k_L$	0.4764
		$R_L$	0.0402–0.2956

The best mathematical fit to the experimental data was achieved with the Langmuir model, with a correlation coefficient ( $R^2$ ) of approximately 98% (Table 4). Furthermore, the theoretical maximum adsorption capacity calculated with this model was  $0.0413 \text{ mg} \cdot \text{cm}^{-2}$ , which is relatively close to the experimental value of  $0.0342 \text{ mg} \cdot \text{cm}^{-2}$  for the saturated adsorption capacity.

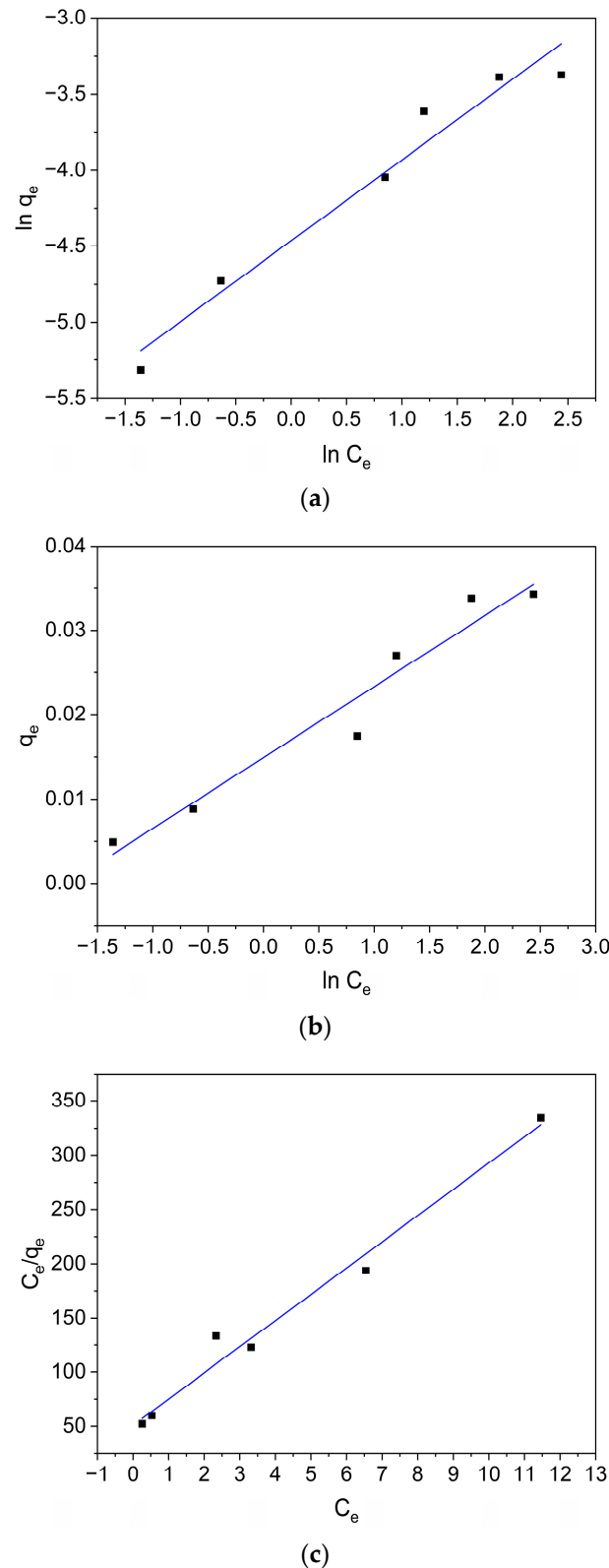


**Figure 6.** Linear representation of the different models of adsorption isotherms: (a) the Freundlich, (b) the Temkin, and (c) the Langmuir models.

Taking into account the fundamental assumptions of the Langmuir model, the adsorption of EBT onto AAO involves the formation of a monolayer of dye molecules on the surface of the sorbent. This requires that the adsorption energy at all active sites of the adsorbent be uniform and that there be no lateral interactions between the adsorbed molecules [15]. These results can be contrasted with the SEM image in Figure 1c. The

complete and homogeneous stacking of EBT molecules on the AAO surface could be assimilated to a single dye layer on the adsorbent surface, which was explained by the Langmuir model.

On the other hand, the Langmuir isotherm can be explained using the dimensionless constant separation factor ( $R_L$ ) [51,52], defined according to the following equation:

$$R_L = \frac{1}{1 + k_L C_0} \quad (7)$$

Depending on the value of the constant  $R_L$ , the favorability of adsorption or efficiency of adsorption process can be defined, with irreversible adsorption when  $R_L = 0$ , favorable when  $0 < R_L < 1$ , linear adsorption when  $R_L = 1$  and unfavorable when  $R_L > 1$  [15,17,53].

Since all  $R_L$  values obtained in the experiments were greater than zero and less than unity, the adsorption processes under the conditions analyzed are favorable. Furthermore, Table 4 shows that as the initial dye concentration increases, the  $R_L$  value approaches zero. This could indicate that the adsorption process tends to be irreversible at higher EBT concentrations [30].

On the other hand, the magnitude of the Freundlich exponent ( $n^{-1}$ ) can also be used as an indicator of the favorability of adsorption, since it is a measure of the strength of adsorption [54,55]. If  $0.1 < n^{-1} < 1$  it can be said that the process is favorable. Based on the results in Table 4, favorable adsorption is again verified ( $n^{-1} = 0.5616$ ).

Likewise, the analysis can be performed taking into account the heterogeneity factor ( $n$ ), whose value in the range of 2–10 means good, 1–2 moderately difficult, and less than 1 poor adsorption characteristics [56–58]. Although the  $n$  obtained was 1.8811, its proximity to the value 2 may indicate relatively low difficulty and favorable adsorption. These results are consistent with those obtained with the Langmuir model.

Finally, the Temkin isotherm model presented the lowest correlation coefficient ( $R^2 = 0.9521$ ), indicating an unsatisfactory fit to the experimental data.

### 3.2.4. Thermodynamic Analysis of the Process

The spontaneity and feasibility of the adsorption process can be determined by calculating the thermodynamic parameters  $\Delta G^\circ$ ,  $\Delta H^\circ$ , and  $\Delta S^\circ$ . To this end, adsorption tests were carried out at different temperatures (25, 40, 50, and 60 °C) and at an initial EBT concentration of 16 mg·L<sup>−1</sup>.

The thermodynamic parameter values displayed in Table 5 were determined using Equations (4)–(6) described in Section 2.4.4 and the data fitting represented in Figure 7.

**Table 5.** Thermodynamic parameters of adsorption process ( $C_0 = 16 \text{ mg} \cdot \text{L}^{-1}$ ).

T (°C)	$\Delta G^\circ$ (KJ·mol <sup>−1</sup> )	$\Delta H^\circ$ (KJ·mol <sup>−1</sup> )	$\Delta S^\circ$ (KJ·mol <sup>−1</sup> ·K <sup>−1</sup> )
25	−3.28	73.81	0.26
40	−4.58		
50	−10.39		
60	−11.50		

The negative  $\Delta G^\circ$  values for each temperature observed in Table 5 indicate that the adsorption process is favorable and spontaneous under the conditions analyzed [33]. Furthermore, a decrease in  $\Delta G^\circ$  can be observed as the temperature increases, suggesting that adsorption is more favorable at higher temperatures. This can be contrasted with the results obtained in Section 3.2.1, which explains why the dye removal efficiency naturally increases at higher temperatures [59].



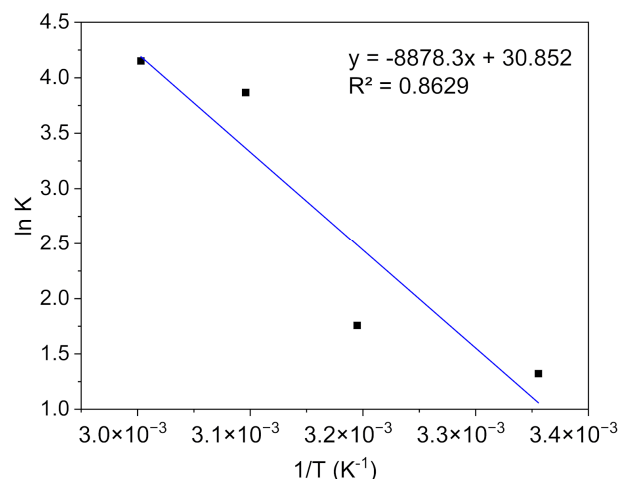


**Figure 7.** Line graph for the determination of thermodynamic parameters.

On the other hand, the positive value of  $\Delta H^\circ$  indicates that the process is endothermic and absorbs energy since the value of  $\Delta H^\circ$  is above  $40 \text{ KJ}\cdot\text{mol}^{-1}$  and nearly  $80 \text{ KJ}\cdot\text{mol}^{-1}$  ( $73.81 \text{ KJ}\cdot\text{mol}^{-1}$ ) this suggests that the adsorption phenomenon is predominantly chemisorption [17,60].

Finally, the positive value of  $\Delta S^\circ$  reflects process stability and randomness at the liquid/solid interface [17].

### 3.2.5. Adsorbent Reuse

The results of the reuse of the AAO (Figure 8) obtained at  $50^\circ\text{C}$  and after two hours of EBT adsorption demonstrated an improvement in the %R during the second and third reuse cycles. This could be due to the modification of the oxide layer by the attack of the NaOH solution used in the dye desorption process [61]. In this sense, the dissolution of the OAA increased the porosity and the specific surface area of the adsorbent. Therefore, new active sites were created. Finally, a decrease in %R could be observed from the fourth use, produced by the progressive dissolution of the OAA and the elimination of the oxide layer with each wash.

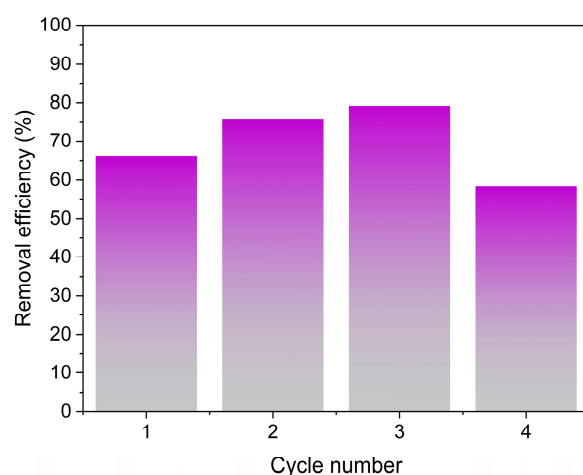


**Figure 8.** Reuse cycles for the AAO at 500 rpm and  $50^\circ\text{C}$  and an initial EBT concentration of  $16 \text{ mg}\cdot\text{L}^{-1}$ .

## 4. Conclusions

In this study, the adsorptive capacity of AAO nanoporous coatings to remove EBT dye from water was demonstrated. The evolution of the adsorption process at different

stirring speeds and temperatures determined that the maximum adsorption capacity of the dye occurred after 2.25 h at 500 rpm and 60 °C, with 99% removal efficiency. The fitting of the data with the proposed kinetic models determined that the adsorption process is controlled by three stages: a slow stage of diffusion of the dye through the boundary layer, a relatively rapid stage of adsorption of the dye molecules in the active sites and a stage of internal diffusion until saturation equilibrium is reached. The Langmuir isotherm model provided the best fit, suggesting the formation of a homogeneous monolayer of dye molecules and the favorability of adsorption. Thermodynamic analyses indicated that the adsorption process proceeds spontaneously and exothermically. Furthermore,  $\Delta H^\circ$  values demonstrated that EBT adsorption on AAO is primarily controlled by the chemisorption mechanism. Finally, it was demonstrated that the adsorbent can be used up to four times with a removal efficiency greater than 50%.

**Author Contributions:** Conceptualization, G.R.K. and F.A.B.; methodology, G.R.K. and F.A.B.; software, G.R.K. and F.A.B.; formal analysis, G.R.K. and F.A.B.; investigation G.R.K.; resources, A.E.A. and P.D.Z.; writing—original draft preparation, G.R.K. and F.A.B.; writing—review and editing, G.R.K. and F.A.B.; supervision, A.E.A. and P.D.Z.; project administration, A.E.A.; funding acquisition, G.R.K., A.E.A. and P.D.Z. All authors have read and agreed to the published version of the manuscript.

**Funding:** This research was funded by Consejo Nacional de Investigaciones Científicas y Técnicas (CONICET), the Agencia Nacional de Promoción Científica y Tecnológica (ANPCyT) of Argentina (PICT-2021-00881), the Universidad Nacional de Misiones (CUDAP: DISP\_SGCYT-S01:0000389/2022) and also funded by the scholarships from CONICET and the Universidad Nacional de Misiones.

**Institutional Review Board Statement:** Not applicable.

**Informed Consent Statement:** Not applicable.

**Data Availability Statement:** The data presented in this study are available on reasonable request.

**Acknowledgments:** G.R.K. and F.A.B. appreciate the support provided by the Universidad Nacional de Misiones. All authors are grateful to the National Scientific CONICET (Consejo Nacional de Investigaciones Científicas y Técnicas). G.R.K. and F.A.B. wish to thank the following chemical engineering students: Agustina I. Nedel, Lara C. Dwojak, and Rocío M. Bitchatchi for their collaboration in carrying out the essays.

**Conflicts of Interest:** The authors declare no conflicts of interest.

## Abbreviations

The following abbreviations are used in this manuscript:

AAO	Anodic aluminum oxide
EBT	Eriochrome black T
PD	Pore Diameter
D	Pore density
P	Porosity
SEM	Scanning electron microscopy
EDS	Energy-dispersive spectrometer
T	Thickness
PFO	Pseudo first-order model
PSO	Pseudo second-order model
IPD	Intraparticle diffusion model
ED	Boyd's external diffusion model

## References

1. Solmaz, A.; Sari, Z.A.; Karta, M.; Turna, T.; Yücel, A.; Depci, T. Production and Characterization of Activated Carbon from Pomegranate Peel for Pharmaceutical Waste (Paracetamol) Removal: Response Surface Methodology Application. *Water Air Soil Poll.* **2023**, *234*, 645. [\[CrossRef\]](#)
2. Solmaz, A. Adsorption of Methylene Blue and Eriochrome Black T onto Pinecone Powders (*Pinus Nigra* Arn.): Equilibrium, Kinetics, and Thermodynamic Studies. *Processes* **2024**, *12*, 2044. [\[CrossRef\]](#)
3. Rashid, R.; Shafiq, I.; Akhter, P.; Iqbal, M.J.; Hussain, M. A State-of-the-Art Review on Wastewater Treatment Techniques: The Effectiveness of Adsorption Method. *Environ. Sci. Pollut. Res.* **2021**, *28*, 9050–9066. [\[CrossRef\]](#)
4. Diorio, L.A.; Fréchou, D.M.S.; Levin, L.N. Removal of Dyes by Immobilization of *Trametes Versicolor* in a Solid-State Micro-Fermentation System. *Rev. Argent. Microbiol.* **2021**, *53*, 3–10. [\[CrossRef\]](#) [\[PubMed\]](#)
5. Hoppen, M.I.; Carvalho, K.Q.; Ferreira, R.C.; Passig, F.H.; Pereira, I.C.; Rizzo-Domingues, R.C.P.; Lenzi, M.K.; Bottini, R.C.R. Adsorption and Desorption of Acetylsalicylic Acid onto Activated Carbon of Babassu Coconut Mesocarp. *J. Environ. Chem. Eng.* **2019**, *7*, 102862. [\[CrossRef\]](#)
6. Slama, H.B.; Chenari Bouket, A.; Pourhassan, Z.; Alenezi, F.N.; Silini, A.; Cherif-Silini, H.; Oszako, T.; Luptakova, L.; Golińska, P.; Belbahri, L. Diversity of Synthetic Dyes from Textile Industries, Discharge Impacts and Treatment Methods. *Appl. Sci.* **2021**, *11*, 6255. [\[CrossRef\]](#)
7. Gupta, V.K.; Kumar, R.; Nayak, A.; Saleh, T.A.; Barakat, M.A. Adsorptive Removal of Dyes from Aqueous Solution onto Carbon Nanotubes: A Review. *Adv. Colloid Interface Sci.* **2013**, *193–194*, 24–34. [\[CrossRef\]](#)
8. Yiğit Avdan, Z.; Demirtaş, İ.; Suvacı, E. Improved Photocatalytic Degradation of Methylene Blue by Novel Hexagonal ZnO Particles. *Water SA* **2024**, *50*, 392–403. [\[CrossRef\]](#)
9. Robinson, T.; McMullan, G.; Marchant, R.; Nigam, P. Remediation of Dyes in Textile Effluent: A Critical Review on Current Treatment Technologies with a Proposed Alternative. *Bioresour. Technol.* **2001**, *77*, 247–255. [\[CrossRef\]](#)
10. Kusumlata; Ambade, B.; Kumar, A.; Gautam, S. Sustainable Solutions: Reviewing the Future of Textile Dye Contaminant Removal with Emerging Biological Treatments. *Limnol. Rev.* **2024**, *24*, 126–149. [\[CrossRef\]](#)
11. Yagub, M.T.; Sen, T.K.; Afroze, S.; Ang, H.M. Dye and Its Removal from Aqueous Solution by Adsorption: A Review. *Adv. Colloid Interface Sci.* **2014**, *209*, 172–184. [\[CrossRef\]](#)
12. Sarkar, S.; Banerjee, A.; Halder, U.; Biswas, R.; Bandopadhyay, R. Degradation of Synthetic Azo Dyes of Textile Industry: A Sustainable Approach Using Microbial Enzymes. *Water Conserv. Sci. Eng.* **2017**, *2*, 121–131. [\[CrossRef\]](#)
13. Zafar, S.; Bukhari, D.A.; Rehman, A. Azo Dyes Degradation by Microorganisms—An Efficient and Sustainable Approach. *Saudi J. Biol. Sci.* **2022**, *29*, 103437. [\[CrossRef\]](#)
14. Khalid, A.; Zubair, M.; Ihsanullah. A Comparative Study on the Adsorption of Eriochrome Black T Dye from Aqueous Solution on Graphene and Acid-Modified Graphene. *Arab. J. Sci. Eng.* **2018**, *43*, 2167–2179. [\[CrossRef\]](#)
15. El Gaayda, J.; Akbour, R.A.; Titchou, F.E.; Afanga, H.; Zazou, H.; Swanson, C.; Hamdani, M. Uptake of an Anionic Dye from Aqueous Solution by Aluminum Oxide Particles: Equilibrium, Kinetic, and Thermodynamic Studies. *Groundw. Sustain. Dev.* **2021**, *12*, 100540. [\[CrossRef\]](#)
16. Wong, S.; Ghafar, N.A.; Ngadi, N.; Razmi, F.A.; Inuwa, I.M.; Mat, R.; Amin, N.A.S. Effective Removal of Anionic Textile Dyes Using Adsorbent Synthesized from Coffee Waste. *Sci. Rep.* **2020**, *10*, 2928. [\[CrossRef\]](#) [\[PubMed\]](#)
17. Ballou, I.; Naja, J.; Bakher, Z.; Kholtei, S. Adsorption of Eriochrome Black T on Pseudo Boehmite and Gamma Alumina Synthesized from Drinking Water Treatment Sludge: A Waste-to-Recycling Approach. *Recycling* **2024**, *9*, 49. [\[CrossRef\]](#)
18. Abhinaya, M.; Parthiban, R.; Kumar, P.S.; Vo, D.-V.N. A Review on Cleaner Strategies for Extraction of Chitosan and Its Application in Toxic Pollutant Removal. *Environ. Res.* **2021**, *196*, 110996. [\[CrossRef\]](#)
19. Mittal, A.; Gupta, V.K. Adsorptive Removal and Recovery of the Azo Dye Eriochrome Black T. *Environ. Toxicol. Chem.* **2010**, *92*, 1813–1823. [\[CrossRef\]](#)
20. Khan, A.; Ju, P.; Han, Z.; Ni, C. A Comprehensive Review on Adsorptive Removal of Azo Dyes Using Functional Materials. *AQUA Water Infrastruct. Ecosyst. Soc.* **2024**, *73*, 266–285. [\[CrossRef\]](#)
21. Sardar, M.; Manna, M.; Maharana, M.; Sen, S. Remediation of Dyes from Industrial Wastewater Using Low-Cost Adsorbents. In *Green Adsorbents to Remove Metals, Dyes and Boron from Polluted Water*; Inamuddin, A.M.I., Lichtfouse, E., Asiri, A.M., Eds.; Environmental Chemistry for a Sustainable World; Springer International Publishing: Cham, Switzerland, 2021; Volume 49, pp. 377–403. [\[CrossRef\]](#)
22. Wang, J.; Guo, X. Adsorption Isotherm Models: Classification, Physical Meaning, Application and Solving Method. *Chemosphere* **2020**, *258*, 127279. [\[CrossRef\]](#) [\[PubMed\]](#)
23. Cavalcante, L.C.; De Carvalho, K.Q.; Bassetti, F.J.; Coral, L.A.A. Kinetic, Isothermal and Thermodynamic Studies of Reactive Black 5 Removal Using Rice Husk Ashes and Powdered Activated Carbon. *Desalin. Water. Treat.* **2024**, *320*, 100606. [\[CrossRef\]](#)

24. Fernandes, E.P.; Silva, T.S.; Carvalho, C.M.; Selvasembian, R.; Chaukura, N.; Oliveira, L.M.T.M.; Meneghetti, S.M.P.; Meili, L. Efficient Adsorption of Dyes by  $\gamma$ -Alumina Synthesized from Aluminum Wastes: Kinetics, Isotherms, Thermodynamics and Toxicity Assessment. *J. Environ. Chem. Eng.* **2021**, *9*, 106198. [\[CrossRef\]](#)
25. Wang, B.; Hu, Y.; Xie, L.; Peng, K. Biosorption Behavior of Azo Dye by Inactive CMC Immobilized *Aspergillus Fumigatus* Beads. *Bioresour. Technol.* **2008**, *99*, 794–800. [\[CrossRef\]](#)
26. Uddin, M.J.; Ampiaiw, R.E.; Lee, W. Adsorptive Removal of Dyes from Wastewater Using a Metal-Organic Framework: A Review. *Chemosphere* **2021**, *284*, 131314. [\[CrossRef\]](#)
27. Bruera, F.A.; Kramer, G.R.; Vera, M.L.; Ares, A.E. Synthesis and Morphological Characterization of Nanoporous Aluminum Oxide Films by Using a Single Anodization Step. *Coatings* **2019**, *9*, 115. [\[CrossRef\]](#)
28. Bruera, F.A.; Kramer, G.R.; Vera, M.L.; Ares, A.E. Evaluation of the Influence of Synthesis Conditions on the Morphology of Nanostructured Anodic Aluminum Oxide Coatings on Al 1050. *Surf. Interfaces* **2020**, *18*, 100448. [\[CrossRef\]](#)
29. Bruera, F.A.; Kramer, G.R.; Velázquez, J.E.; Sadañoski, M.A.; Fonseca, M.I.; Ares, A.E.; Zapata, P.D. Laccase Immobilization on Nanoporous Aluminum Oxide for Black Liquor Treatment. *Surf. Interfaces* **2022**, *30*, 101879. [\[CrossRef\]](#)
30. Li, N.; Li, X.; Yang, Y.; Liu, Y.; Zhao, L.; Zhou, Z. Adsorption-Desorption Behavior of Silver Ions on Stainless Steel as a Proxy for Disinfection of Domestic Hot Water. *Desalin. Water. Treat.* **2019**, *151*, 230–241. [\[CrossRef\]](#)
31. Sharififard, H.; Soleimani, M. Performance Comparison of Activated Carbon and Ferric Oxide-Hydroxide-Activated Carbon Nanocomposite as Vanadium (v) Ion Adsorbents. *RSC Adv.* **2015**, *5*, 80650–80660. [\[CrossRef\]](#)
32. Muliwa, A.M.; Oyewo, O.A.; Maity, A. Recent Progress on the Removal of Aqueous Mercury by Carbon-Based Adsorbents: A Review. *Inorg. Chem. Commun.* **2023**, *156*, 111207. [\[CrossRef\]](#)
33. Chatla, A.; Almanassra, I.W.; Kochkodan, V.; Laoui, T.; Alawadhi, H.; Atieh, M.A. Efficient Removal of Eriochrome Black T (EBT) Dye and Chromium (Cr) by Hydrotalcite-Derived Mg-Ca-Al Mixed Metal Oxide Composite. *Catalysts* **2022**, *12*, 1247. [\[CrossRef\]](#)
34. Ahmaruzzaman, M.; Laxmi Gayatri, S. Batch Adsorption of 4-Nitrophenol by Acid Activated Jute Stick Char: Equilibrium, Kinetic and Thermodynamic Studies. *Chem. Eng. J.* **2010**, *158*, 173–180. [\[CrossRef\]](#)
35. Jamhour, R.M.A.Q.; Al-Msideen, A.; Al-Faraheed, R.; Esaifan, M.; Jamhour, M. Adsorptive Removal of Hazardous Eriochrome Black T and Its Metal Complexes from Aqueous Media Using Spent Coffee Grounds. *Res. Sq.* **2023**. [\[CrossRef\]](#)
36. Sangor, F.I.M.S.; Al-Ghouti, M.A. Waste-to-Value: Synthesis of Nano-Aluminum Oxide (Nano- $\gamma$ -Al<sub>2</sub>O<sub>3</sub>) from Waste Aluminum Foils for Efficient Adsorption of Methylene Blue Dye. *Case Stud. Chem. Environ. Eng.* **2023**, *8*, 100394. [\[CrossRef\]](#)
37. Goswami, R.; Goswami, Y.C.; Shahrestasni, M. Synthesis and Characterization of Aluminium Oxide Nano Adsorbents via a Sustainable Combustion Method for Methyl Red Remediation. *Rev. Roum. Chim.* **2024**, *69*, 595–603. [\[CrossRef\]](#)
38. Kyzas, G.Z.; Favvas, E.P.; Kostoglou, M.; Mitropoulos, A.C. Effect of Agitation on Batch Adsorption Process Facilitated by Using Nanobubbles. *Colloids Surf. A Physicochem. Eng. Asp.* **2020**, *607*, 125440. [\[CrossRef\]](#)
39. Kuśmierek, K.; Świątkowski, A. The Influence of Different Agitation Techniques on the Adsorption Kinetics of 4-Chlorophenol on Granular Activated Carbon. *Reac. Kinet. Mech. Cat.* **2015**, *116*, 261–271. [\[CrossRef\]](#)
40. Dharmarathna, S.P.; Priyantha, N. Investigation of Boundary Layer Effect of Intra-Particle Diffusion on Methylene Blue Adsorption on Activated Carbon. *Energy Nexus* **2024**, *14*, 100294. [\[CrossRef\]](#)
41. Boudouaia, N.; Bengharez, Z.; Jellali, S. Preparation and Characterization of Chitosan Extracted from Shrimp Shells Waste and Chitosan Film: Application for Eriochrome Black T Removal from Aqueous Solutions. *Appl. Water Sci.* **2019**, *9*, 91. [\[CrossRef\]](#)
42. Saber-Samandari, S.; Gulcan, H.O.; Saber-Samandari, S.; Gazi, M. Efficient Removal of Anionic and Cationic Dyes from an Aqueous Solution Using Pullulan-Graft-Polyacrylamide Porous Hydrogel. *Water Air Soil Pollut.* **2014**, *225*, 2177. [\[CrossRef\]](#)
43. Lafi, R.; Montasser, I.; Hafiane, A. Adsorption of Congo Red Dye from Aqueous Solutions by Prepared Activated Carbon with Oxygen-Containing Functional Groups and Its Regeneration. *Adsorp. Sci. Technol.* **2019**, *37*, 160–181. [\[CrossRef\]](#)
44. Bansal, M.; Patnala, P.K.; Dugmore, T. Adsorption of Eriochrome Black-T(EBT) Using Tea Waste as a Low Cost Adsorbent by Batch Studies: A Green Approach for Dye Effluent Treatments. *Curr. Res. Green Sustain. Chem.* **2020**, *3*, 100036. [\[CrossRef\]](#)
45. Chebbi, M.; Ounoki, S.; Youcef, L.; Amrane, A. Synthesis and Characterization of Pine Cones Biochar for the Removal of an Antibiotic (Metronidazole) from Aqueous Solutions. *J. Ind. Eng. Chem.* **2023**, *126*, 327–339. [\[CrossRef\]](#)
46. Wang, J.; Guo, X. Adsorption Kinetic Models: Physical Meanings, Applications, and Solving Methods. *J. Hazard. Mater.* **2020**, *390*, 122156. [\[CrossRef\]](#) [\[PubMed\]](#)
47. Ahmed, M.J.; Theydan, S.K. Microwave Assisted Preparation of Microporous Activated Carbon from Siris Seed Pods for Adsorption of Metronidazole Antibiotic. *Chem. Eng. J.* **2013**, *214*, 310–318. [\[CrossRef\]](#)
48. Ghibate, R.; Senhaji, O.; Taouil, R. Kinetic and Thermodynamic Approaches on Rhodamine B Adsorption onto Pomegranate Peel. *Case Stud. Chem. Environ. Eng.* **2021**, *3*, 100078. [\[CrossRef\]](#)
49. Kecira, Z.; Benturki, O.; Benturki, A.; Daoud, M.; Girods, P. High Adsorption Capacity of Nitrobenzene from Aqueous Solution Using Activated Carbons Prepared from Vegetable Waste. *Env. Prog. Sustain. Energy* **2020**, *39*, e13463. [\[CrossRef\]](#)
50. Randhawa, N.S.; Das, N.N.; Jana, R.K. Adsorptive Remediation of Cu(II) and Cd(II) Contaminated Water Using Manganese Nodule Leaching Residue. *Desalin. Water Treat.* **2014**, *52*, 4197–4211. [\[CrossRef\]](#)

51. Zheng, H.; Liu, D.; Zheng, Y.; Liang, S.; Liu, Z. Sorption Isotherm and Kinetic Modeling of Aniline on Cr-Bentonite. *J. Hazard. Mater.* **2009**, *167*, 141–147. [[CrossRef](#)]
52. El Amri, A.; Bensalah, J.; Kadiri, L.; Essaadaoui, Y.; Lebkiri, I.; Zarrouk, A.; Rifi, E.H.; Lebkiri, A. Investigation of the Cellulose Reed Plant as a Potential Adsorbent to Remove Pb(II): Equilibrium Isotherms and Thermodynamic Studies. *Desalin. Water Treat.* **2022**, *262*, 137–151. [[CrossRef](#)]
53. Singh, R.K.; Kumar, S.; Kumar, S.; Kumar, A. Development of Parthenium Based Activated Carbon and Its Utilization for Adsorptive Removal of P-Cresol from Aqueous Solution. *J. Hazard. Mater.* **2008**, *155*, 523–535. [[CrossRef](#)] [[PubMed](#)]
54. Ifelebuegu, A.O. Removal of Steroid Hormones by Activated Carbon Adsorption—Kinetic and Thermodynamic Studies. *J. Environ. Prot.* **2012**, *03*, 469–475. [[CrossRef](#)]
55. Jasper, E.E.; Ajibola, V.O.; Onwuka, J.C. Nonlinear Regression Analysis of the Sorption of Crystal Violet and Methylene Blue from Aqueous Solutions onto an Agro-Waste Derived Activated Carbon. *Appl. Water Sci.* **2020**, *10*, 132. [[CrossRef](#)]
56. Li, X.; Wang, J.; Zhang, X.; Chen, C. Powdered Activated Carbon Adsorption of Two Fishy Odorants in Water: Trans, Trans-2,4-Heptadienal and Trans,Trans-2,4-Decadienal. *J. Environ. Sci. Int.* **2015**, *32*, 15–25. [[CrossRef](#)]
57. Treybal, R.E. *Mass Transfer Operations*, 3rd ed.; McGraw Hill: New York, NY, USA, 1980.
58. Carvalho, M.; Duque, A.; Goncalves, I.; Castro, P. Adsorption of Fluorobenzene onto Granular Activated Carbon: Isotherm and Bioavailability Studies. *Bioresour. Technol.* **2007**, *98*, 3424–3430. [[CrossRef](#)]
59. Lutfullah; Rashid, M.; Haseen, U.; Rahman, N. An Advanced Cr(III) Selective Nano-Composite Cation Exchanger: Synthesis, Characterization and Sorption Characteristics. *J. Ind. Eng. Chem.* **2014**, *20*, 809–817. [[CrossRef](#)]
60. Labaali, Z.; Kholtei, S.; Naja, J. Co<sup>2+</sup> Removal from Wastewater Using Apatite Prepared through Phosphate Waste Rocks Valorization: Equilibrium, Kinetics and Thermodynamics Studies. *Sci. Afr.* **2020**, *8*, e00350. [[CrossRef](#)]
61. Asoh, H.; Fukumoto, S.; Shishido, K.; Hagiwara, K. Anodization of Aluminum in a Sodium Hydroxide Solution: Effect of pH on Chemical Dissolution. *J. Electrochem. Soc.* **2024**, *171*, 123504. [[CrossRef](#)]

**Disclaimer/Publisher’s Note:** The statements, opinions and data contained in all publications are solely those of the individual author(s) and contributor(s) and not of MDPI and/or the editor(s). MDPI and/or the editor(s) disclaim responsibility for any injury to people or property resulting from any ideas, methods, instructions or products referred to in the content.